Nanoscale

Accepted Manuscript

This article can be cited before page numbers have been issued, to do this please use: W. Xiong, R. Jiang, W. Sun, X. Peng, S. Bi and C. Chen, *Nanoscale*, 2025, DOI: 10.1039/D5NR02015H.

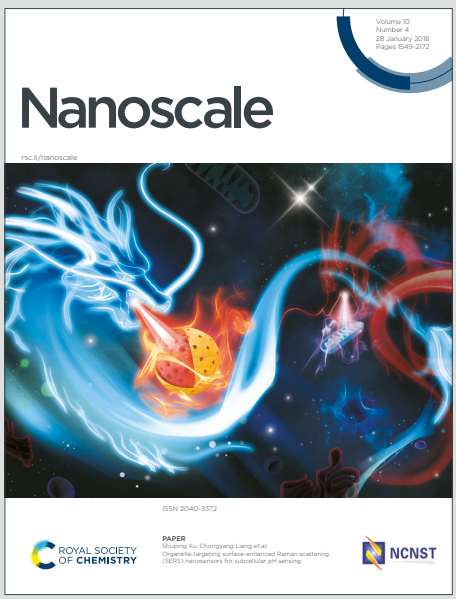

ROYAL SOCIETY OF CHEMISTRY

rsc.li/nanoscale

View Article Online
DOI: 10.1039/D5NR02015H

Femtosecond Laser Constructed Bioinspired Gradient Wedge-Shaped Surfaces for Under-Oil Liquid Self-Transport

Wei Xiong[1], Ruisong Jiang[1],Weixin Sun[1], Xuqiao Peng[1], Shuai Bi[1], Chaolang Chen[1]*

1: School of Mechanical Engineering, Sichuan University, Chengdu, China, 610065

*: C.C.(chaolangchen@scu.edu.cn)

Abstract: The spontaneous transport of liquids holds significant application potential in biomedicine, heat dissipation, microfluidic chips, and so forth. Particularly, the under-oil liquid self-transport is a significant pathway for manipulating the volatile liquids. Although numerous functional surfaces have been developed to facilitate the directional self-transport of liquids (e.g., water, oil) in the air, reports on the self-transport of liquids in oily environments remain scarce. Herein, inspired by the lotus leaves and cactus spines, we propose a bionic superwetting gradient wedge-shaped surface (SGWS) for under-oil self-transport of liquids. The SGWS was fabricated through a combination of femtosecond laser texturing and hydrophobic modification. The as-prepared SGWS can achieve fast and continuous self-transport of a single droplet under-oil, exhibiting a maximal transport velocity of over 250 mm/s and transport distance of over 150 mm. The effect of wedge-shaped angle, inclined angle, and surface tension on the self-transport behavior of liquid on the SGWS was systematically investigated and the underlying mechanism was revealed. Furthermore, the potential applications of the SGWS in complex fluid manipulation, droplet microchemical reactions, cargo transport, and oil surface particles collection were explored in detail. This work offers a novel strategy for realizing under-oil liquid manipulation without energy input, showing promising applications in the industry.

1. Introduction

Manipulation of liquids has been extensively applied in biomedicine,[1–4] material identification,[5–8] microfluidic control,[9–14]and so forth. Particularly, the manipulation of liquids within oily environments holds significant research value. For instance, manipulating toxic gases or volatile liquids in the air will result in fast evaporation and

View Article Online
DOI: 10.1039/D5NR02015H

mass loss, threatening the environment and human health. Manipulating those toxic gases (Dissolved in an aqueous solution) and volatile liquids in an oily environment is an efficient way to reduce harm and avoid liquid evaporation. Therefore, developing advanced methods for the manipulation of liquids under oil has important academic significance and industrial value.[15–17]

Liquid manipulation can be achieved through external energy input[18–24] or gradient surface-based liquid self-transport.[3,10,25–31] Among them, achieving the self-transport of liquids by bionic gradient surface has attracted wide attention due to its advantages of simple structure, low energy consumption, and easy operation. Recently, inspired by natural biological structures (e.g., cactus spines or desert beetles), various bionic gradient surfaces, such as conical surfaces, wedge-shaped surfaces, and wettability gradient surfaces, have been developed for the self-transport of liquids in air.[9,25,32–41] However, rare research about under-oil liquid self-transport is reported. Since the surface energy of oil is lower than that of water, the oil is more likely to wet object surfaces than water. This results in water having difficulty directly contacting object surfaces under-oil, thereby preventing water from using structural gradients to achieve self-transport. Additionally, because water droplets move under-oil, they must overcome the viscous resistance of the oil. Therefore, for water moving under-oil, it must overcome the difficulty of water not easily wetting the surface of objects and the viscous resistance generated during movement. Some studies in recent years have also successfully achieved the self-transport of water droplets under-oil.[34–36] Yu et al.[35] fabricated a TiO_2-coated conical spine and subsequently endowed it with underwater superhydrophilic properties via UV irradiation. The TiO_2-coated conical spine achieved the self-transport of under-oil liquid without water prewetting, exhibiting a short transport distance of ~3 mm and a low speed of ~1 mm/s. In our previous work, inspired by the structure of cactus spines, a conical copper needle with superhydrophilic properties was fabricated, which can achieve the self-transport of under-oil water droplets via water pre-wetting, exhibiting a transport distance of ~33 mm.[36] Although existing researches have achieved self-transport of liquids under-oil, the limited transport distance, complex prewetting procedure, and curved surface-based driven

View Article Online
DOI: 10.1039/D5NR02015H

method greatly restrict their application in practical liquid manipulation. Therefore, there is an urgent need to develop advanced methods to achieve the rapid, long-distance self-transport of under-oil liquids on the two-dimensional platform.

Herein, to address the above challenge, a superwetting gradient wedge-shaped surface (SGWS) was proposed for under-oil liquid self-transport. The SGWS was fabricated by combining femtosecond laser processing and surface modification. The self-transport behavior of under-oil liquid on the as-prepared SGWS was systematically investigated and the underlying mechanism was revealed. The as-prepared SGWS can realize the fast, long-distance, and continuous self-transport of liquid in different types of oil environments. In addition, the potential application of the as-prepared SGWS in droplet microchemical reactions, cargo transport, and oil surface particles collection was demonstrated. This work presents a novel strategy for the self-transport of under-oil liquids, providing fresh design concepts and inspiration in the area of microfluidic and liquid manipulation.

2. Results and Discussion

2.1 The Design and Characterization of the SGWS

In nature, the micro-nano mastoid structures on the upper surface of the lotus leaf endow it with excellent superhydrophobic properties.[42] The tapered spines of cactus can realize the spontaneous self-transport of fog via the curved surface-based Laplace pressure gradient.[43] Inspired by the lotus leaves and cactus spines, a superwetting gradient wedge-shaped surface (SGWS) was designed for the self-transport of under-oil liquid. As shown in Figure 1a, the designed SGWS contains a wedge-shaped pattern with superhydrophilic properties and a lotus-inspired area with superhydrophobic properties.

View Article Online
DOI: 10.1039/D5NR02015H

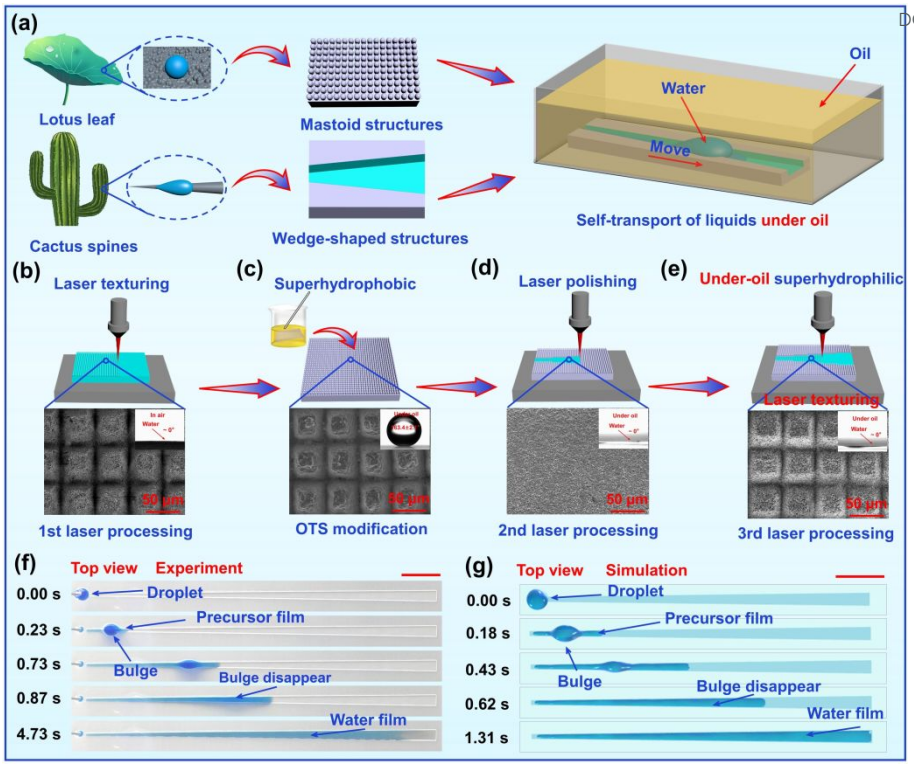

Figure 1. (a) The design of SGWS was inspired by the mastoid structures on the surface of the lotus leaf and the conical cluster of thorns on the stem of the cactus. (b-e) Fabrication schematic of the SGWS, the SEM, and the water contact angle (WCA) images of the substrate surface after each procedure. Snapshot of the under-oil liquid self-transport on the SGWS: (f) experiment results (Top view, wedge-shaped angle of 1.4°); (g) simulation results (Top view, wedge-shaped angle of 1.4°). Scale bar, 10 mm.

The quartz glass possesses intrinsic under-oil hydrophilicity due to the high surface energy of SiO_2 and the abundant surface polar group (-OH) on its surface.[44,45] Hence, to endow the wedge-shaped pattern with under-oil superhydrophilic properties, the quartz glass was selected as a substrate to fabricate SGWS. The fabrication process of SGWS was illustrated in Figure 1b-e and Table S1 (Supporting Information). First, periodic bionic mastoid structures were constructed on the quartz glass via femtosecond laser texturing (Inset of Figure 1b). The quartz glass transformed from hydrophilic (Figure S1a, Supporting Information) to superhydrophilic. Second, the laser-textured quartz glass was hydrophobically modified via grafting octadectyltrichlorosilane (OTS) self-assembled film (Figure 1c). EDS spectrum of laser-textured glass showed that the

View Article Online
DOI: 10.1039/D5NR02015H

mass fraction of the C (Carbon) element increased from 9.13% to 34.06% after OTS modification (Figure S2a-c, Supporting Information), confirming the successful grafting of the OTS self-assembled film. The OTS-modified textured glass exhibited a WCA of ~ 154.2°±1.5° in the air (Figure S1b, Supporting Information) and ~ 163.4°±2.1° under-oil (Figure 1c), showing outstanding superhydrophobicity. Third, a smooth and superhydrophilic wedge-shaped channel was constructed on the OTS-modified textured glass via laser polishing to remove the OTS modification and mastoid structures (Figure 1d). EDS spectrum of the laser-polishing area shows that the mass fraction of the C element decreased from 34.06% to 11.62% (Figure S2d, Supporting Information), confirming the complete removal of the OTS film. The laser-polishing area became superhydrophilic under oil. Finally, new bionic mastoid structures were constructed on the wedge-shaped channel via secondary laser texturing (Figure 1e). The new bionic mastoid area exhibited superoleophilicity in air (Figure S3a, Supporting Information) and superhydrophilicity. However, due to the inherent characteristics of quartz glass (High surface energy and abundant polar groups), this region exhibits superhydrophilicity under-oil and superoleophobicity underwater.[45] That is, in the region with the new mastoid structures, water can rapidly spread out under-oil (Figure S3b, Supporting Information), while oil cannot underwater (Figure S3c, Supporting Information). As compared with the smooth channel surface, the channel with mastoid structures could enhance the wetting and spread of liquid (Figure S4, Supporting Information). The optical image of the as-prepared SGWS is shown in Figure S5 (Supporting Information). It can be seen that the appearance of a wedge-shaped channel was whitish, while the superhydrophobic background was darker. The laser scanning confocal microscope (LSCM) image showed that the micro-mastoid structures in the SGWS superhydrophobic region have a height of ~39.35 μm, and the micro-mastoid structures within the superhydrophilic channel exhibit a height of ~26.28 μm, with the channel depth measuring ~116.32 μm (Figure S6, Supporting Information).

The self-transport behavior of under-oil liquid on the as-prepared SWGS was observed experimentally. First, the as-prepared SGWS was immersed in the oil phase (N-dodecane. Unless otherwise specified, all droplets moved in n-dodecane). Then, a

water droplet was released at the narrow side of the SGWS by the precision liquid syringe, and the dynamic behavior of the droplet was recorded by a video camera. To enhance visualization, the water droplets were stained with methylene blue. As shown in Figure 1f, it can be seen that once the water droplet (25 μL) contacted the tip of the wedge-shaped channel, it immediately formed a liquid precursor film in front of the droplet (Figure S7a and Movie S1 in Supporting Information). The droplet's bulge became thinner and elongated as it moved along the wedge-shaped channel. Eventually, the droplet's bulge completely spread and fused with the liquid precursor film at a distance of 39.27 mm at 0.87s. Subsequently, the precursor film kept moving forward and eventually stopped at the channel position of 90 mm at 4.73s (Figure S8, Supporting Information).

Further, the self-transport behavior of under-oil liquid on the SGWS was numerically studied through a two-phase coupling phase field simulation method (Detailed simulation parameters were shown in Note S1, supporting information). As shown in Figure 1g and Figure S7b (Supporting Information), it can be seen that similar phenomena including the formation and transport of precursor transport film and bulge were observed in the simulation results, which are highly consistent with the experimental results, demonstrating that the precursor film plays a crucial role for driving the droplet to transport on the wedge-shaped channel. After the first droplet's movement, a thin layer of water film covered the entire superhydrophilic channel of the SGWS. On this basis, the second droplet moved faster compared to the first one (Figures S9 and S10, Supporting Information). This is because the water film was formed on the channel after the first droplet moved over, which reduced volume loss for the subsequent droplets, and acts as a lubricant film.

It can be seen from the processing of SGWS that the depth of the superhydrophilic channel ($\triangle h$) and the spacing between the mastoid structures within the channel (D) are important factors affecting the movement performance of water droplets under-oil. Therefore, we prepared SGWS with different $\triangle h$ and D by using different laser powers and different scanning spacings to explore their influence on the droplet movement performance (Figure 2a and b).

View Article Online
DOI: 10.1039/D5NR02015H

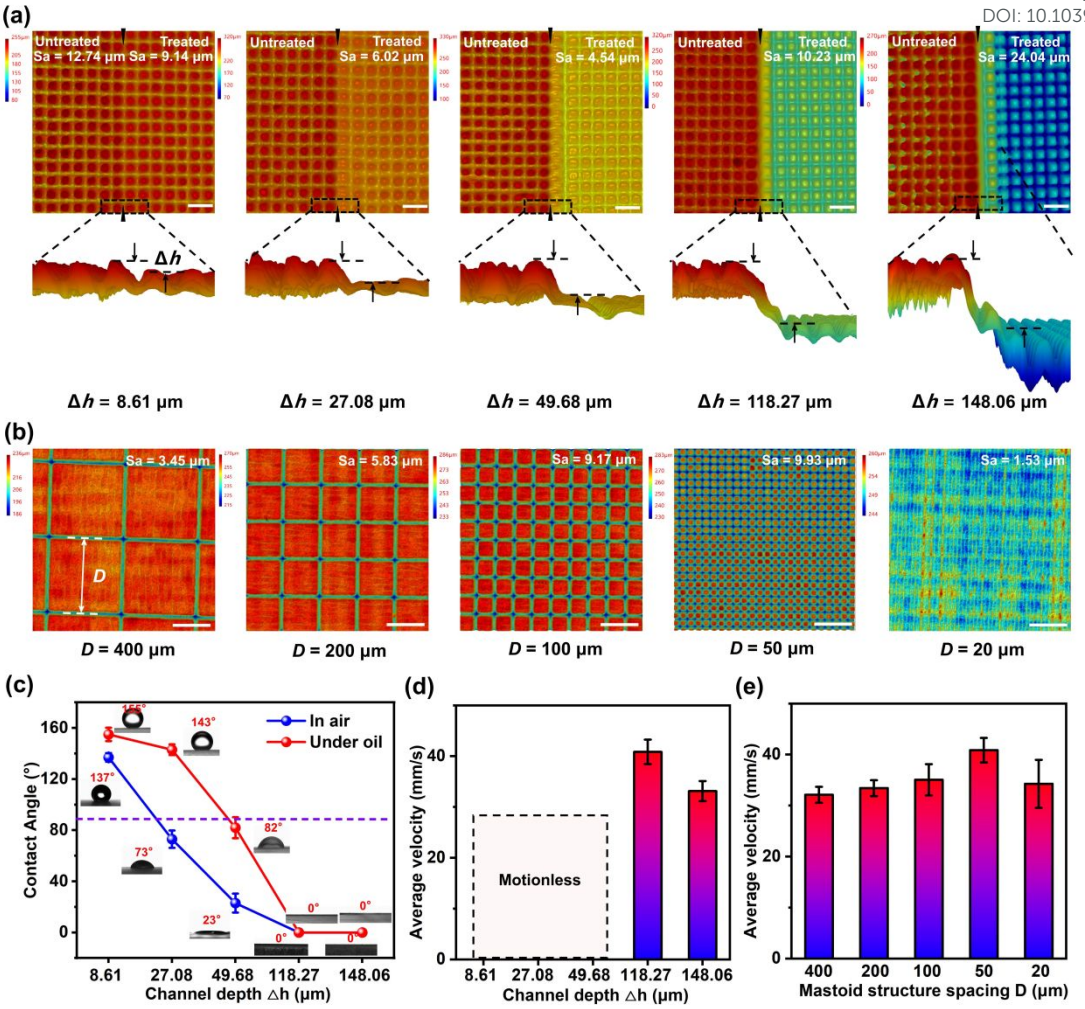

Figure 2. (a) LSCM images of quartz surfaces under different $\triangle h$ conditions. $\triangle h$ = 8.61, 27.08, 49.68, 118.27, 148.06 μm were prepared using laser powers of 4.4, 5.2, 6.1, 10.0, and 12.0 W, respectively. At this time, D = 50 μm. Sa represents surface roughness. Scale bar, 100 μm. (b) LSCM images of quartz surfaces under different D conditions. The laser scanning intervals were 400, 200, 100, 50, and 20 μm in sequence. At this time, the laser power = 10.0 W. Scale bar, 200 μm. (c) The surface wettability after processing superhydrophobic quartz glass at different laser powers. (d) The average velocity of droplet movement on the SGWS under different laser powers (V = 40 μL, α = 1.4°, L = 90 mm, D = 50 μm). (e) The average velocity of droplet movement on the SGWS under different laser scanning intervals (V = 40 μL, α = 1.4°, L = 90 mm, laser processing power = 10.0 W).

Different $\triangle h$ could be obtained by using different laser processing powers. Figure 2a shows SLCM images with different $\triangle h$ processed successively using laser powers

of 4.4, 5.2, 6.1, 10.0, and 12.0 W. The greater the power of the laser, the greater its $\triangle h$. At the laser power = 4.4 W, $\triangle h$ = 8.61 μm, the Sa decreased from 12.74 μm (Untreated area) to 9.14 μm. At this point, the WCA of the treated surface was ~137°, while the under-oil WCA was ~155° (Figure 2c), preventing droplets from moving on the channel (Figure S11a, Supporting Information). At the laser powers = 5.2 W and 6.1 W, $\triangle h$ gradually increased, and Sa gradually decreased. Despite the hydrophilicity of the processed areas (WCA ~ 73° and ~23°, respectively), droplets could not reach the end of the channels due to their under oil WCA ~143° and ~82° (Figure S11b and c, Supporting Information), respectively. When the laser power reached 10.0 W, $\triangle h$ = 118.27 μm, the Sa of the processed region rose to 10.23 μm, and the wettability achieved under-oil superhydrophilicity. Consequently, the droplets could move quickly under the oil along the channel to the end (Figure 2d and S11d, Supporting Information). However, when the laser power was increased to 12.0 W, the Sa and $\triangle h$ increased significantly to 24.04 μm and 148.06 μm, respectively, due to the excessive power. As a result, the droplet was consumed at a significantly faster rate during its movement, resulting in a decrease in its travel speed (Figure S11e, Supporting Information).

Subsequently, we investigated the effect of the spacing between different papillary structures within the superhydrophilic channel on droplet movement performance (Figure 2b). Different *D* values were obtained using different laser scanning intervals. The laser scanning interval and *D* are in a corresponding relationship (When the laser scanning interval is 50 μm, *D* is 50 μm). As shown in Figure 2e, as *D* decreased from 400 μm to 20 μm, the average movement speed of the droplets first increased and then decreased. This can be explained as follows: as *D* decreased from 400 μm to 50 μm, the number of papillae structures per unit area increased, Sa increased, and the wettability of the droplets was enhanced, thereby increasing the average movement speed. However, when *D* was further reduced to 20 μm, significant overlap occurred between adjacent microchannels (The laser spot diameter ~30 μm), causing the basic microchannel structure to disappear, and Sa decreased instead. Therefore, the average motion velocity at *D* = 20 μm was lower than that at 50 μm. Unless otherwise specified, the SGWS was prepared at 10.0 W and *D* = 50 μm throughout the article.

As shown in Figure S12 (Supporting Information), the second droplet exhibited a maximum velocity of 256.76 mm/s and a transport distance of over 90 mm, showing exceptional performance in the under-oil self-transport of liquids. As shown in Figure S13 and Table S2 (Supporting Information), compared with the reported underwater self-transport systems for water droplets in previous literature,[34–36] the as-proposed SGWS by this work achieved the fast, long-distance transport of under-oil liquid on a two-dimensional platform for the first time.

2.2 Effect of Droplet Volume, Wedge-Shaped Angle, Droplet Types, and Oil Types on Droplet Motion Performance

To further understand the underlying mechanism of the self-transport of under-oil droplets on the SGWS, the forces exerted on the droplet during its self-transport process on the SGWS were analyzed and discussed in detail. As shown in Figure 3a, when the droplet came in contact with the tip of the wedge-shaped channel of the SGWS, the droplet tended to spread on the channel under the drive of the capillary wetting force (F_C), which led to a rapid formation of a precursor film in front of the droplet. Besides, the droplet on the precursor film tends to form an asymmetrical bulge shape under the action of the asymmetrical wettability gradient force (F_W) generated from the boundary between the superhydrophilic wedge-shaped channel and the outside superhydrophobic area. The asymmetrical surface curve of the bulge shape generated an unbalanced Laplace force (F_L) on the droplet, which drove it to move from the tip side to the base side of the wedge-shaped channel. During the movement of droplet and precursor film on the SGWS, hysteresis drag (F_H) and fluid viscous drag (F_D) play as resistance to restrain the movement.[9,27,44,46–49] Detailed mechanical analysis was shown in Note S2 of (Supporting Information). It can be seen that the forces exerted on the droplet are mainly affected by the droplet size, the wedge-shaped angle, the surface tension, and the viscous resistance of oil, which further dominate the transport of underoil liquid on SGWS.

View Article Online
DOI: 10.1039/D5NR02015H

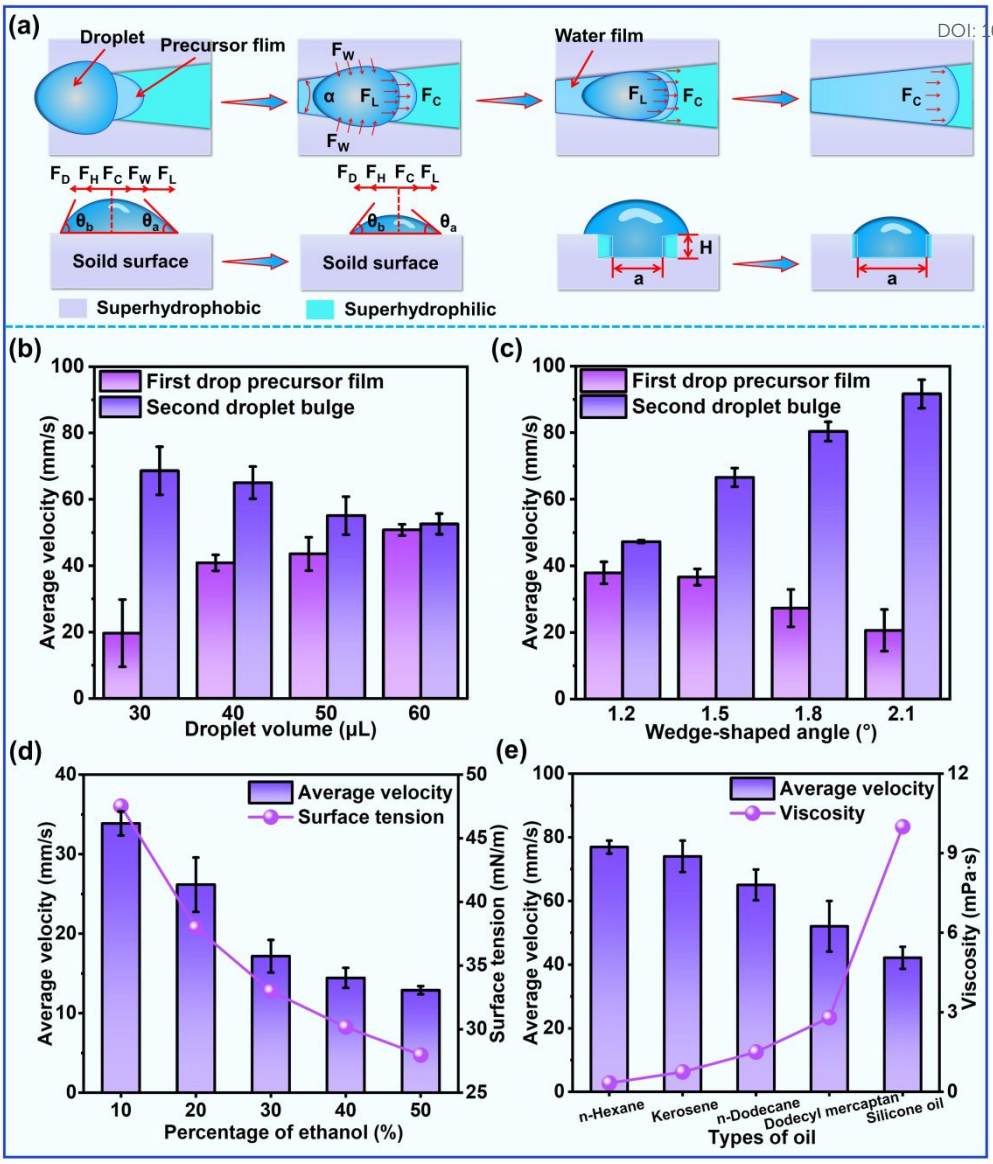

Figure 3. (a) Mechanical analysis of under-oil liquid self-transport on the SGWS. (b) The relationship between the droplet average velocity and the droplet volume (α = 1.4°, L = 90 mm). (c) The relationship between the droplet average velocity and the wedge-shaped angle (V = 45 μL, L = 90 mm). (d) The relationship between the droplet average velocity and the percentage of ethanol (V = 40 μL, α = 1.4°, L = 90 mm). (e) The relationship between the droplet average velocity and the different types of oil (V = 40 μL, α = 1.4°, L = 90 mm).

The moving velocity of the first droplet's precursor film and the second droplet bulge varies with the droplet volume, as shown in Figure 3b and Figure S14 (Supporting Information). It can be seen that the moving velocity of the droplet precursor film increased with the increase of droplet volume. This is because the larger droplets have

View Article Online
DOI: 10.1039/D5NR02015H

higher surface energy, which accelerates the spreading of the droplet on the SGWS. Besides, the moving velocity of the second droplet bulge decreased with the increase of droplet volume, which can be attributed to the larger droplet possessing higher viscous resistance. Subsequently, we further investigated the relationship between the number of droplets and the average movement speed by continuously adding droplets (Figure S15, Supporting Information). The moving velocity of the first droplet's precursor film and the second droplet varies with the wedge-shaped angle of the SGWS, as shown in Figure 3c and Figure S16 (Supporting Information). It can be seen that the moving velocity of the first droplet's precursor film decreased with the increase of the wedge-shaped angle of the SWGS. This is because when the wedge-shaped angle of SGWS is larger, it increases volume consumption, thereby reducing movement speed. Moreover, the moving velocity of the second droplet bulge increased with the increase of the wedge-shaped angle of the SGWS. This is because a higher asymmetrical curvature was generated on the front and rear surfaces of the droplet when it was placed on the SGWS with a higher wedge angle, which generated a larger Laplace force to promote the movement of the droplet on the SGWS. Finally, by measuring the average speed of droplets from the first to the 50th droplet on the SGWS, we demonstrated the excellent robustness of the SGWS (Figure S17, Supporting Information).

Besides, the relationship between surface tension and droplet movement performance was investigated. Liquids with different surface tensions were created by adding different amounts of anhydrous ethanol to deionized water. As shown in Figure 3d, the results indicate that the average velocity of the liquid's movement decreases as the concentration of the ethanol solution increases. This can be attributed to the lower surface tension resulting in reduced Laplace force on the droplet, which consequently leads to a decrease in the moving velocity of the droplet on the SGWS. In addition, the moving velocity of droplets on the SWGS in different oil environments was evaluated. As shown in Figure 3e, the results show that the moving velocity of the droplet is highly related to the viscosity of the oil phase. The droplet moves faster in an oil with lower viscosity. This can be attributed to the higher the viscosity, the higher the resistance the droplet experiences while moving, which leads to a lower moving velocity of the

droplet on the SWGS. In addition, the self-transport of liquid in heavy oil (Taking dichloromethane with a density of 1.325 g/cm^3 as an example) was studied. As shown in Figure S18 (Supporting Information), the under-oil liquid can be spontaneously and continuously transported on both the horizontal SGWS and the inclined SGWS. Meanwhile, a droplet with a specific size can be separated from the end of SGWS under the action of buoyancy (Movie S2, Supporting Information), which provides a concept to produce microdroplets in the oil phase.

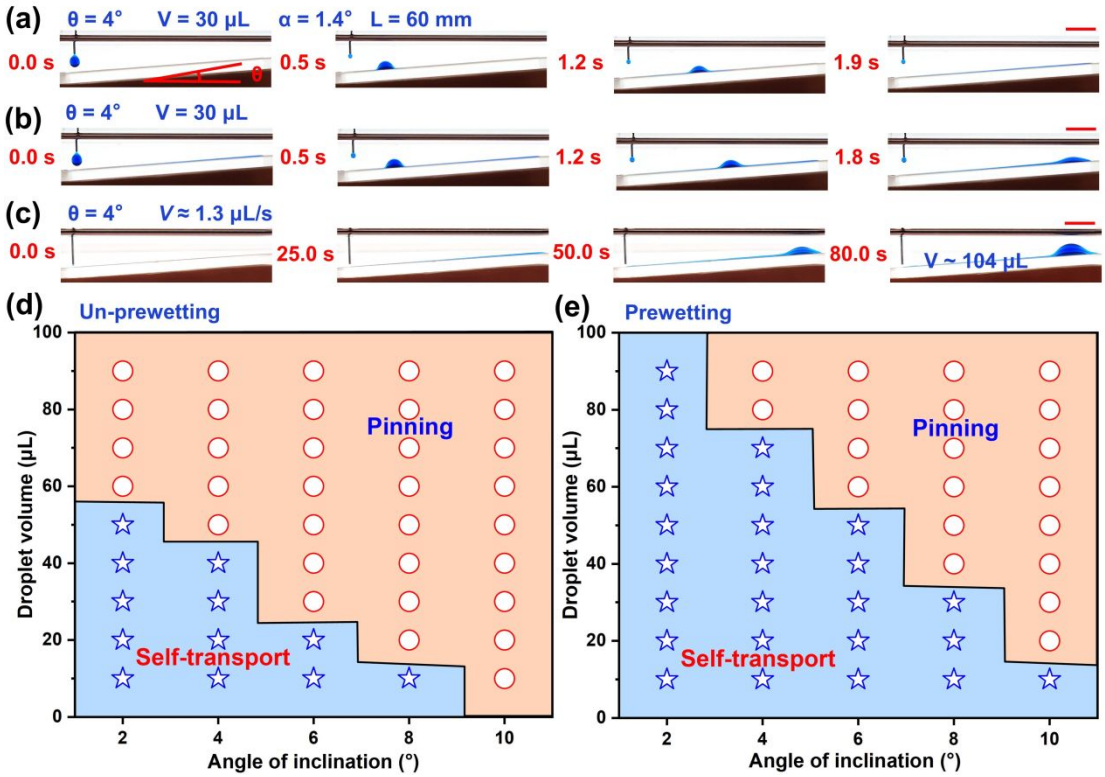

Figure 4. Snapshots of the (a) first droplet and (b) second droplet moving on the inclined SGWS under-oil (n-dodecane). (c) Continuous transport of under-oil (n-dodecane) liquid on the inclined SGWS. (d) The critical volume of droplet self-transport on the un-prewetting SGWS with different inclination angles (α = 1.4°, L = 60 mm). (e) The critical volume of droplet self-transport on the prewetting SGWS with different inclination angles (α = 1.4°, L = 60 mm).

Moreover, the movement of droplets on the inclined SWGS was investigated. Figures 4a and b show the optical images of a water droplet with a volume of 30 μL transported on the channel with a tilt angle of 4° and a length of 60 mm (Part 1 of Movie S3, Supporting Information). When the first spherical water droplet on the syringe came

into contact with the superhydrophilic channel, it immediately moved rapidly along the channel. With the increasing displacement of the movement, the droplet bulge continually became thinner and lengthened, and reached the end of displacement at 1.9 s (Figure 4a). Meanwhile, the second droplet had a similar motion to the first droplet and moved to the end of the channel at t = 1.8 s (Figure 4b). Besides, the under-oil liquid can be continuously upward transported on the inclined SGWS as shown in Figure 4c. A total of ~104 μL of liquid was transported from the tip of the SGWS to the base of the SGWS (Part 2 of Movie S3, Supporting Information).

In addition, the critical volumes of droplets for self-transportation at tilt angles of 2°, 4°, 6°, 8°, and 10° were recorded by statistical analysis. The critical volume is defined as the maximum volume of droplets that can self-transport on the SGWS at a specific inclination angle. As shown in Figure 4 (d, e), it can be seen that the droplet critical volume on the inclined SGWS decreased with the increase in inclination angle, which has nothing to do with whether the SGWS is prewetted. This is because the component of droplet gravity in the direction of droplet motion is increased with the increase of the SGWS's inclination angle, which plays a role in resisting to inhibit the self-transport of droplets. Furthermore, due to the water film formed on the SGWS surface through prewetting (~10 μL of water pre-moved along the channel), the movement resistance and volume loss during subsequent droplet movement were reduced, enabling droplets to move more easily along the channel. Therefore, at the same tilt angle, the critical volume of droplets on prewetting SGWS was higher than that on un-prewetting SGWS.

2.3 Complex Fluid Manipulation and Potential Applications Based on SGWS.

In this section, the potential applications of the as-prepared SGWS in complex fluid manipulation, microchemical reactions, cargo transport, and oil surface cleanup were studied and discussed. As shown in Figure 5, structured surfaces based on SGWS were designed and fabricated to verify their potential application in under-oil complex microfluidic tasks such as splitting, merging, and long-distance transport. As shown in Figure 5a, a continuous liquid splitting can be realized on a designed "structured pattern" based on the SGWS (Part 1 of Movie S4, Supporting Information). Besides, a "Y"-

shaped surface based SGWS was constructed for under-oil droplet mixing as shown in Figure 5b. When two droplets with different concentrations were released simultaneously at the end of "Y"-shaped channel, and the droplets spontaneously moved toward the intersection of the channel, and merged upon contact, forming a large fluid bulge there. The merged fluid bulge is continuously transported to the end of the "Y"-shaped channel (Part 2 of Movie S4, Supporting Information). In addition, as shown in Figure 5c, an SGWS-based channel was designed to achieve the long-distance self-transport of under-oil liquids on a 2D planar platform. The results indicate that the under-oil liquids can be continuously transported on the SGWS-based channel with a transport distance over 150 mm (Part 3 of Movie S4, Supporting Information).

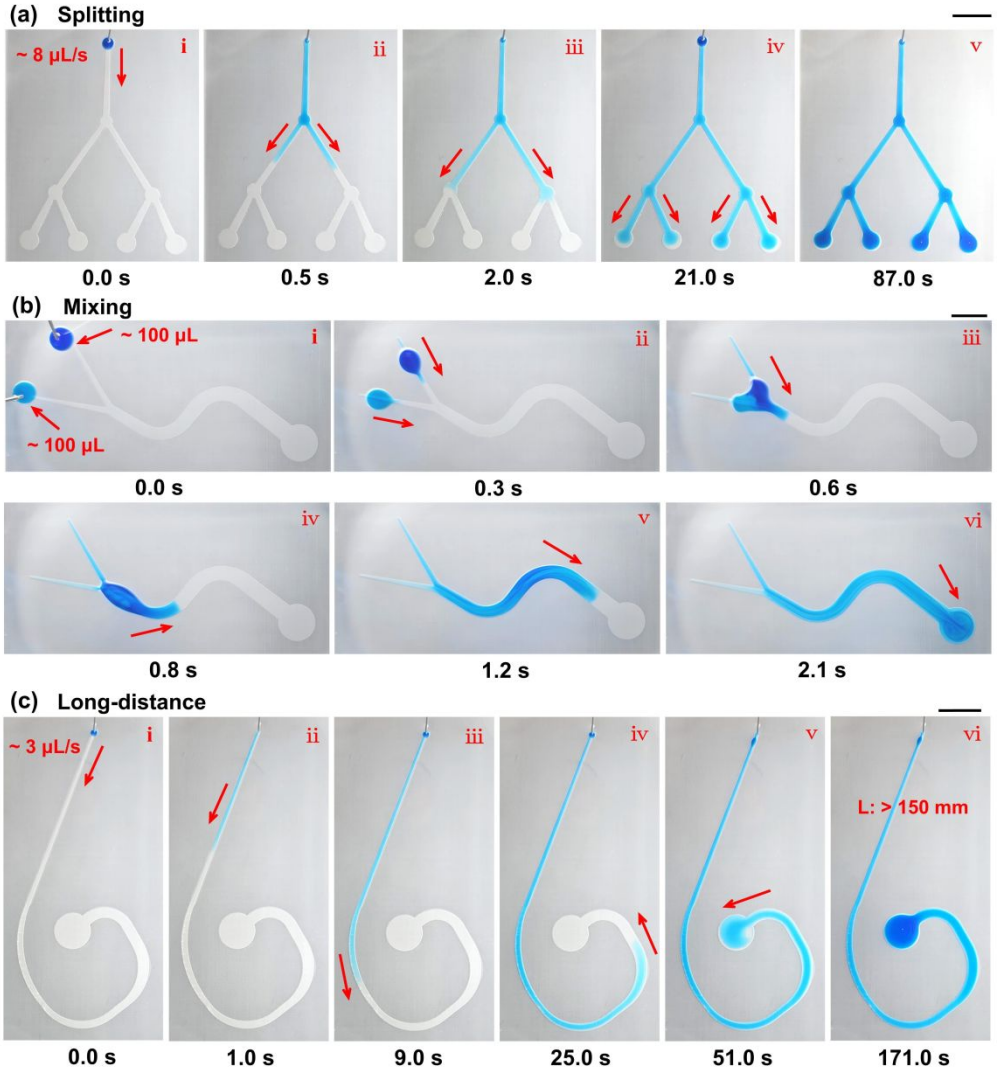

Figure 5. Optical images of the SGWS-based functional surfaces for complex microfluidic manipulation. (a) Splitting, (b) mixing, (c) long-distance of under-oil

View Article Online
DOI: 10.1039/D5NR02015H

liquids. Scale bar, 10 mm.

Moreover, a microfluidic pattern based on SGWS was designed for under-oil microchemical reactions (Figure S19, Supporting Information). The SGWS-based microfluidic pattern consists of wedge-shaped transport channels on both sides and a circular reaction area in the middle. The SGWS-based microfluidic pattern can be used to identify the acidity and alkalinity of the solution. As shown in Figure 6a and Movie S5 (Supporting Information), a litmus droplet (~ 50 μL) was first placed on the circular reaction area in the middle of the SGWS-based microfluidic pattern. Subsequently, a hydrochloric acid droplet (w(HCl) = 20%) was released on the tip of the right side SWGS-based microfluidic pattern. It can be seen that the hydrochloric acid droplet spontaneously transported toward the reaction zone and merged with the litmus. It can be seen that the color of the merged solution changed from purple to pink, indicating that the hydrochloric acid solution was acidic. Subsequently, a droplet of ammonia solution (w(NH_3) = 10%) was released on the tip of the left side SWGS-based microfluidic pattern. It can be seen that the ammonia solution droplet spontaneously transported toward the reaction zone and merged with the solution. The color of the merged solution changed from pink to blue, indicating that the ammonia solution was alkaline. This device offers a strategy for detecting harmful gases and volatile liquids to reduce material consumption and environmental pollution, showing a broad application prospect.

View Article Online
DOI: 10.1039/D5NR02015H

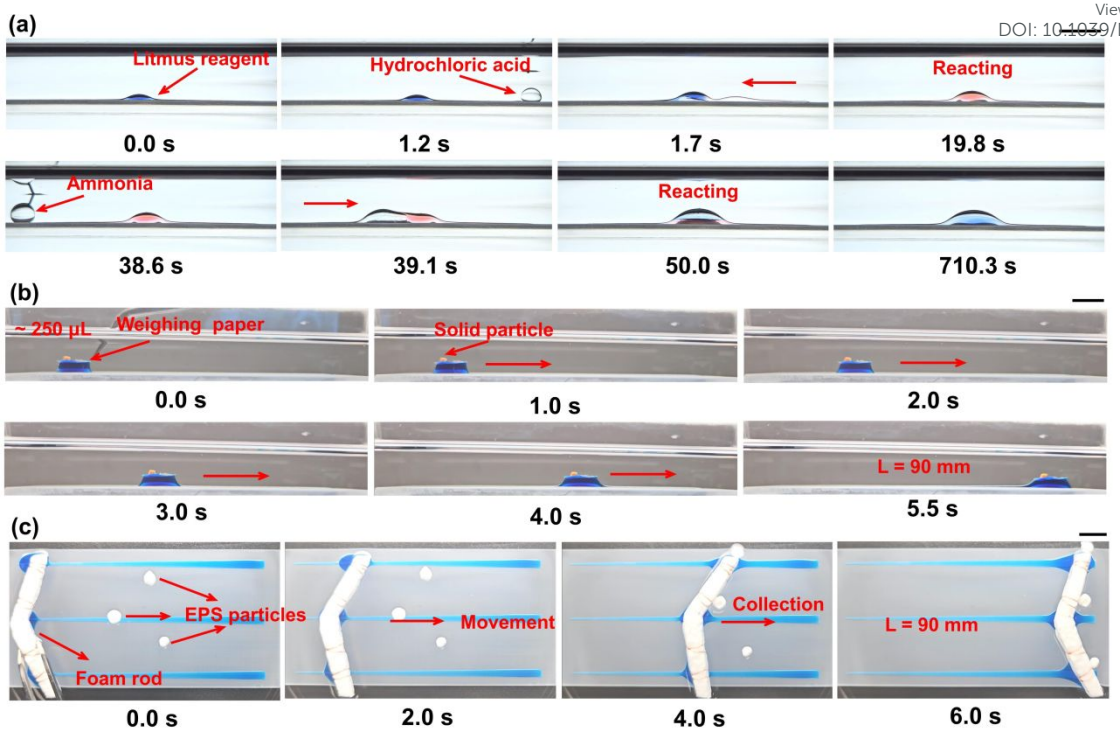

Figure 6. (a) Snapshots of chemical microreactions under-oil using the SGWS-based system. (b) Snapshots of cargo transport using the SGWS-based system. (c) Snapshots of particles collection on the oil surface using the SGWS-based system. Scale bar, 10 mm.

In addition, a SGWS-based liquid conveyor was constructed to transport under-oil solid particles by placing a weighing paper on the droplet (Figure S20, Supporting Information). The transport of solid particles on the SGWS-based liquid conveyor was assessed. As shown in Figure 6b, a 3D-printed particle (Polyethylene Terephthalate Glycol-modified, < 0.01 g) was placed on the liquid conveyor to demonstrate the transport of the solid particle, and the liquid conveyor was placed on the narrow side of SGWS and fixed by a tweezer. After removing the tweezer, the liquid conveyor carrying the solid particle spontaneously transported from the narrow side to the wide side of the SGWS system (Movie S6, Supporting Information).

Besides, as shown in Figure S21 and Part 1 of Movie S7 (Supporting Information), it was found that the SGWS-based system can realize the self-transport of a simi-immersed droplet (Partially immersed in the oil and partially exposed to the air). Based on the concept of a liquid conveyor, it can be used for the collection and transportation of particles on the oil surface. An oil surface particle collection device was constructed

View Article Online
DOI: 10.1039/D5NR02015H

by aligning three SGWS-based channels (Figure S22 and S23, Supporting Information). A foam rod was placed on the droplet and fixed by a tweezer on the narrow side of the SGWS-based surface. As shown in Figure 6c, after removing the tweezer, the foam rod spontaneously moved toward the wide side of the SGWS-based surface. Subsequently, the expandable polystyrene particles floating on the surface of the oil were collected and transported to the wide side of the SGWS-based surface (Part 2 of Movie S7, Supporting Information). The SGWS-based system could be employed for a wide range of applications such as complex liquid manipulation, microfluid chips, droplet micro-reaction, and cargo transport.

3 Conclusion

In this research, inspired by the mastoid structures of lotus leaf surfaces and cactus spines, superwetting gradient wedge-shaped surfaces (SGWS) were prepared on quartz glass by combining femtosecond laser processing and octadecyltrichlorosilane (OTS) chemical modification techniques, and applied for the self-transport of liquids under-oil. The as-prepared SGWS achieved a maximum transport velocity of over 250 mm/s and a transport distance of over 150 mm. It was observed that during the liquid's self-transport, the first droplet movement generates a water film that significantly reduces resistance for subsequent droplets, thereby improving the second droplet's velocity. Additionally, the volume of the droplet, the wedge-shaped angle, surface tension, and the viscosity of the oil have an important influence on the droplet's movement performance. Building on the realization of complex fluid manipulation, including splitting, mixing, and long-distance curved self-transport, the SGWS-based system has also successfully achieved under-oil chemical microreaction, cargo transport, and oil-surface particles collection. This research enhances the understanding of liquid manipulation and provides a new strategy for developing high-performance under-oil liquid self-transport systems.

4 Materials and Methods

4.1 Materials

The n-hexane, n-dodecane, dichloromethane, dodecyl mercaptan, silicone oil, and

View Article Online
DOI: 10.1039/D5NR02015H

trichlorooctadecylsilane (OTS) used in the experiment were purchased from Saan Chemical Technology (Shanghai) Co., Ltd. Anhydrous ethanol was purchased from Chengdu Lixinhe Chemical Co., Ltd. Quartz glass, kerosene, and deionized water were purchased from BOE.

4.2 Preparation of SGWS

The SGWS was prepared by combining femtosecond laser (FemtoYL-20, Anyang, Wuhan) processing and chemical modification, utilizing quartz glass as its substrate. First, an array of lotus leaf papillae-like structures with an interval of 50 μm was fabricated on the quartz glass at a scanning speed of 50 mm/s for one time, using the laser with a pulse width of 300 fs, frequency of 500 kHz, power of 10 W, and wavelength of 1030 nm. And then the quartz glass was scanned 3 additional times at a scanning speed of 200 mm/s. Subsequently, the quartz glass after laser processing was ultrasonically cleaned using anhydrous ethanol for 10 min and then dried. Second, the quartz glass was immersed in a mixed solution (40 ml of n-hexane was mixed with 2 ml of OTS, stirred for 2 minutes, and then 10 μL of deionized water was added and stirred again for 1 minute) for chemical modification for 40 minutes. Then, the as-prepared sample was dried at 60 ℃ for 60 minutes to obtain the superhydrophobic surfaces. Third, the laser, moving at a scanning speed of 1000 mm/s and an interval of 3 μm, was used to polish the localized surface of the sample 3 times to remove the OTS modification and obtain the superhydrophilic wedge-shaped channels. Finally, the sample was processed 3 times at a scanning speed of 200 mm/s and a scanning interval of 50 μm with the remaining laser parameters unchanged, and the superhydrophilic wedge-shaped corner structure was obtained after laser processing five times at a scanning speed of 500 mm/s.

4.3 Characterization

The trajectory of a droplet moving on the surface of the SGWS was captured by a mobile phone (Galaxy S23, Samsung) at a rate of 60 fps. The velocity of the droplet was obtained from the analysis of its position by employing Tracker software. The surface morphology images of the sample were taken by a field emission electron microscope system (SEM, SU8220, Apreo) and Laser Scanning Confocal Microscopy

(LSCM, OLS4100, Olympus). Elemental analysis was carried out by energy dispersive spectroscopy (EDS, Bruker). The water contact angle (WCA) was measured by using a dynamic contact angle meter (Dataphysics, OCA15, Germany) at room temperature. The volume of water droplets used in the WCA measurements was 4 μL. The WCA was measured 3 times and averaged.

4.4 Simulation

A simulation study of the self-transporting system beneath oil was conducted. This study was utilized to elucidate the experimental motion trend through the application of equations. The equation explanations and parameter settings of the simulation model are detailed in Note S1 (Supporting Information).

Author contributions

Wei Xiong: conceptualization, methodology, investigation, and writing – original draft. Ruisong Jiang: validation and visualization. Weixin Sun: writing – original draft, investigation, methodology, and software. Xuqiao Peng: methodology and formal analysis. Shuai Bi: methodology and formal analysis. Chaolang Chen: funding acquisition, resources, supervision, and writing – review & editing.

This manuscript was written through contributions from all authors. All authors have given approval to the final version of the manuscript.

Acknowledgments

The authors thank the financial support from the National Natural Science Foundation of China (No. 52205211), the Natural Science Foundation of Sichuan Province (2025ZNSFSC1280), and the Sichuan University Interdisciplinary Innovation Fund.

Conflicts of Interest

There are no conflicts to declare.

References

(1) Zhang, Y.; Li, J.; Xiang, L.; Wang, J.; Wu, T.; Jiao, Y.; Jiang, S.; Li, C.; Fan, S.; Zhang, J.; Wu, H.; Zhang, Y.; Bian, Y.; Zhao, K.; Peng, Y.; Zhu, W.; Li, J.; Hu, Y.; Wu, D.; Chu, J.; Wang, Z. A Biocompatible Vibration-Actuated Omni-Droplets

Rectifier with Large Volume Range Fabricated by Femtosecond Laser. *Adv. Mater.* **2022**, *34* (12), 2108567. https://doi.org/10.1002/adma.202108567.

(2) Wang, S.; Lee, J. S.; Wahiduzzaman, M.; Park, J.; Muschi, M.; Martineau-Corcos, C.; Tissot, A.; Cho, K. H.; Marrot, J.; Shepard, W.; Maurin, G.; Chang, J.-S.; Serre, C. A Robust Large-Pore Zirconium Carboxylate Metal–Organic Framework for Energy-Efficient Water-Sorption-Driven Refrigeration. *Nat. Energy* **2018**, *3* (11), 985–993. https://doi.org/10.1038/s41560-018-0261-6.

(3) Huang, S.; Li, J.; Liu, L.; Zhou, L.; Tian, X. Lossless Fast Drop Self-Transport on Anisotropic Omniphobic Surfaces: Origin and Elimination of Microscopic Liquid Residue. *Adv. Mater.* **2019**, *31* (27), 1901417. https://doi.org/10.1002/adma.201901417.

(4) Ye, M.; Xue, Y.; Zhao, H.; Hazelton, P.; Ji, Y.; McHale, G.; Chen, X. Programmable Optical Window Bonding Enabled 3D Printing of High-Resolution Transparent Microfluidic Devices for Biomedical Applications. *Droplet* **2025**, *4* (1), e153. https://doi.org/10.1002/dro2.153.

(5) Miao, J.; Tsang, A. C. H. Reconfigurability-Encoded Hierarchical Rectifiers for Versatile 3D Liquid Manipulation. *Adv. Sci.* **2024**, *11* (39), 2405641. https://doi.org/10.1002/advs.202405641.

(6) Sun, S.; Miao, J.; Tan, R.; Zhang, T.; Li, G.; Shen, Y. Asymmetric Soft-Structure Functional Surface for Intelligent Liquids' Distinction, Transportation, and Reaction Mixer. *Adv. Funct. Mater.* **2023**, *33* (1), 2209769. https://doi.org/10.1002/adfm.202209769.

(7) Qu, Y.; Ma, Z.; Zhang, M.; Huang, X.; Xuan, L.; Ding, R.; Liao, W.; Wu, Z.; Lin, Y.; Hu, K.; Liu, Z.; Chen, R.; He, H. Sugar Detection Using Drop Evaporation. *Droplet* **2025**, *4* (1), e150. https://doi.org/10.1002/dro2.150.

(8) Danesh, N.; Torabinia, M.; Moon, H. Droplet Menisci Recognition by Deep Learning for Digital Microfluidics Applications. *Droplet* **2025**, *4* (1), e151. https://doi.org/10.1002/dro2.151.

(9) Xie, D.; Zhang, B. Y.; Wang, G.; Sun, Y.; Wu, C.; Ding, G. High-Performance Directional Water Transport Using a Two-Dimensional Periodic Janus Gradient Structure. *Small Methods* **2022**, *6* (12), 2200812. https://doi.org/10.1002/smtd.202200812.

(10) Liu, Z.; Liu, H.; Li, W.; Song, J. Optimization of Bioinspired Surfaces with Enhanced Water Transportation Capacity. *Chem. Eng. J.* **2022**, *433*, 134568. https://doi.org/10.1016/j.cej.2022.134568.

(11) Yan, D.; Lu, Y.; Liu, J.; Chen, Y.; Sun, J.; Song, J. Enhanced Water Transportation on a Superhydrophilic Serial Cycloid-Shaped Pattern. *Nanoscale* **2023**, *15* (27), 11473–11481. https://doi.org/10.1039/D3NR02180G.

(12) Zhao, C.; Suh, Y.; Won, Y. DropletMask: Leveraging Visual Data for Droplet Impact Analysis. *Droplet* **2024**, *3* (4), e137. https://doi.org/10.1002/dro2.137.

(13) Li, M.; Yu, H.; Liu, Z.; Gao, Z.; Chen, F. Quantitative Liquid Storage by Billiards-like Droplet Collision on Surfaces with Patterned Wettability. *Droplet* **2024**, *3* (3), e125. https://doi.org/10.1002/dro2.125.

(14) Zhang, J.; Chen, Y.; Zhang, Y.; Wu, S.; Sun, J.; Liu, X.; Song, J. Fabrication and Energy Collection of Superhydrophobic Ultra-Stretchable Film. *Adv. Funct. Mater.*

View Article Online
DOI: 10.1039/D5NR02015H

2024, *34* (27), 2400024. https://doi.org/10.1002/adfm.202400024.
(15) Ma, Y.; Liang, Z.; Chen, Y.; Wang, J. Advances in Precise Cell Manipulation. *Droplet* **2025**, *4* (1), e149. https://doi.org/10.1002/dro2.149.
(16) Wu, S.; Yan, D.; Chen, Y.; Song, J. Self-Driven Oil/Water Separator with Super-High Separation Rate. *Nano Energy* **2024**, *119*, 109066. https://doi.org/10.1016/j.nanoen.2023.109066.
(17) Ma, J.; Zhang, C.; Zhang, P.; Song, J. One-Step Synthesis of Functional Slippery Lubricated Coating with Substrate Independence, Anti-Fouling Property, Fog Collection, Corrosion Resistance, and Icephobicity. *J. Colloid Interface Sci.* **2024**, *664*, 228–237. https://doi.org/10.1016/j.jcis.2024.03.027.
(18) Li, A.; Li, H.; Li, Z.; Zhao, Z.; Li, K.; Li, M.; Song, Y. Programmable Droplet Manipulation by a Magnetic-Actuated Robot. *Sci. Adv.* **2020**, *6* (7), eaay5808. https://doi.org/10.1126/sciadv.aay5808.
(19) Miao, J.; Sun, S.; Zhang, T.; Li, G.; Ren, H.; Shen, Y. Natural Cilia and Pine Needles Combinedly Inspired Asymmetric Pillar Actuators for All-Space Liquid Transport and Self-Regulated Robotic Locomotion. *ACS Appl. Mater. Interfaces* **2022**, *14* (44), 50296–50307. https://doi.org/10.1021/acsami.2c12434.
(20) Manabe, K.; Saito, K.; Nakano, M.; Ohzono, T.; Norikane, Y. Light-Driven Liquid Conveyors: Manipulating Liquid Mobility and Transporting Solids on Demand. *ACS Nano* **2022**, *16* (10), 16353–16362. https://doi.org/10.1021/acsnano.2c05524.
(21) Tan, S.; Han, X.; Sun, Y.; Guo, P.; Sun, X.; Chai, Z.; Jiang, L.; Heng, L. Light-Induced Dynamic Manipulation of Liquid Metal Droplets in the Ambient Atmosphere. *ACS Nano* **2024**, *18* (11), 8484–8495. https://doi.org/10.1021/acsnano.4c00690.
(22) Jing, X.; Chen, H.; Shang, X.; Zhang, L.; Zhao, S.; Zhou, X.; Liu, X.; Wang, Z.; Wang, Y.; Du, W.; Guo, Y.; Jiang, L. Photothermal-Electric Excited Droplet Multibehavioral Manipulation. *Adv. Funct. Mater. n/a* (n/a), 2410612. https://doi.org/10.1002/adfm.202410612.
(23) Jin, Y.; Xu, W.; Zhang, H.; Li, R.; Sun, J.; Yang, S.; Liu, M.; Mao, H.; Wang, Z. Electrostatic Tweezer for Droplet Manipulation. *Proc. Natl. Acad. Sci. U. S. A.* **2022**, *119* (2), e2105459119. https://doi.org/10.1073/pnas.2105459119.
(24) Yong, J.; Li, X.; Hu, Y.; Peng, Y.; Cheng, Z.; Xu, T.; Wang, C.; Wu, D. Triboelectric 'Electrostatic Tweezers' for Manipulating Droplets on Lubricated Slippery Surfaces Prepared by Femtosecond Laser Processing. *Int. J. Extreme Manuf.* **2024**, *6* (3), 035002. https://doi.org/10.1088/2631-7990/ad2cdf.
(25) Zhang, X.; Ben, S.; Zhao, Z.; Ning, Y.; Li, Q.; Long, Z.; Yu, C.; Liu, K.; Jiang, L. Lossless and Directional Transport of Droplets on Multi-Bioinspired Superwetting V-Shape Rails. *Adv. Funct. Mater.* **2023**, *33* (20), 2212217. https://doi.org/10.1002/adfm.202212217.
(26) Xie, D.; Sun, Y.; Wu, Y.; Wang, K.; Wang, G.; Zang, F.; Ding, G. Engineered Switchable-Wettability Surfaces for Multi-Path Directional Transportation of Droplets and Subaqueous Bubbles. *Adv. Mater.* **2023**, *35* (9), 2208645. https://doi.org/10.1002/adma.202208645.
(27) Wu, W.; Bai, H.; Yang, Y.; Li, G.; Chen, Z.; Tang, C.; Yin, H.; Lai, L.; Liu, J.; Xuan, S.; Song, Y.; Liu, S.; Yin, K.; Cao, M. Sequence Liquid Manipulation on a

Multifunctional Snowflake-Patterned Interface with Dual Unidirectional Wettability. *J. Mater. Chem. A* **2023**, *11* (16), 8873–8885. https://doi.org/10.1039/D3TA01120H.
(28) Ju, J.; Zheng, Y.; Jiang, L. Bioinspired One-Dimensional Materials for Directional Liquid Transport. *Acc Chem Res* **2014**, *47* (8), 2342.
(29) Hu, B.; Duan, Z.; Xu, B.; Zhang, K.; Tang, Z.; Lu, C.; He, M.; Jiang, L.; Liu, H. Ultrafast Self-Propelled Directional Liquid Transport on the Pyramid-Structured Fibers with Concave Curved Surfaces. *J. Am. Chem. Soc.* **2020**, *142* (13), 6111–6116. https://doi.org/10.1021/jacs.9b13286.
(30) Cui, Z.; Xiao, L.; Li, Y.; Zhang, Y.; Li, G.; Bai, H.; Tang, X.; Zhou, M.; Fang, J.; Guo, L.; Liu, S.; Xiao, C.; Cao, M. A Fishbone-Inspired Liquid Splitter Enables Directional Droplet Transportation and Spontaneous Separation. *J. Mater. Chem. A* **2021**, *9* (15), 9719.
(31) Liu, Q.; Su, Q.; Hong, Q.; Lu, Y.; Huang, S.; Feng, K. A Droplet Splitter: Simple, Controlled and Efficient Droplet Splitting Using Superhydrophobic Pyramid Structures. *Droplet n/a* (n/a), e70014. https://doi.org/10.1002/dro2.70014.
(32) Li, Y.; Cui, Z.; Li, G.; Bai, H.; Dai, R.; Zhou, Y.; Jiao, Y.; Song, Y.; Yang, Y.; Liu, S.; Cao, M. Directional and Adaptive Oil Self-Transport on a Multi-Bioinspired Grooved Conical Spine. *Adv. Funct. Mater.* **2022**, *32* (27), 2201035. https://doi.org/10.1002/adfm.202201035.
(33) Li, M.; Hao, J.; Bai, H.; Wang, X.; Li, Z.; Cao, M. On-Chip Liquid Manipulation via a Flexible Dual-Layered Channel Possessing Hydrophilic/Hydrophobic Dichotomy. *ACS Appl. Mater. Interfaces* **2023**, *15* (15), 19773–19782. https://doi.org/10.1021/acsami.3c03275.
(34) Wu, J.; Yin, K.; Li, M.; Wu, Z.; Xiao, S.; Wang, H.; Duan, J.-A.; He, J. Under-Oil Self-Driven and Directional Transport of Water on a Femtosecond Laser-Processed Superhydrophilic Geometry-Gradient Structure. *Nanoscale* **2020**, *12* (6), 4077–4084. https://doi.org/10.1039/C9NR09902F.
(35) Yu, X.; Lai, H.; Kang, H.; Liu, Y.; Wang, Y.; Cheng, Z. Underoil Directional Self-Transportation of Water Droplets on a TiO2-Coated Conical Spine. *ACS Appl. Mater. Interfaces* **2022**, *14* (4), 6274–6282. https://doi.org/10.1021/acsami.1c24815.
(36) Liu, Y.; Peng, X.; Zhu, L.; Jiang, R.; Liu, J.; Chen, C. Liquid-Assisted Bionic Conical Needle for In-Air and In-Oil–Water Droplet Ultrafast Unidirectional Transportation and Efficient Fog Harvesting. *ACS Appl. Mater. Interfaces* **2023**, *15* (51), 59920–59930. https://doi.org/10.1021/acsami.3c14713.
(37) Cheng, X.; Ye, Y.; Li, Z.; Chen, X.; Bai, Q.; Wang, K.; Zhang, Y.; Drioli, E.; Ma, J. Constructing Environmental-Friendly "Oil-Diode" Janus Membrane for Oil/Water Separation. *ACS Nano* **2022**, *16* (3), 4684–4692. https://doi.org/10.1021/acsnano.1c11388.
(38) Huang, S.; Song, J.; Lu, Y.; Chen, F.; Zheng, H.; Yang, X.; Liu, X.; Sun, J.; Carmalt, C. J.; Parkin, I. P.; Xu, W. Underwater Spontaneous Pumpless Transportation of Nonpolar Organic Liquids on Extreme Wettability Patterns. *ACS Appl. Mater. Interfaces* **2016**, *8* (5), 2942–2949. https://doi.org/10.1021/acsami.5b08596.
(39) Ju, J.; Xiao, K.; Yao, X.; Bai, H.; Jiang, L. Bioinspired Conical Copper Wire with Gradient Wettability for Continuous and Efficient Fog Collection. *Adv Mater* **2013**, *25*

View Article Online
DOI: 10.1039/D5NR02015H

(41), 5937.
(40) Guo, Y.; Luo, Y.-Q.; Liu, L.; Ma, C.; Liu, C.; Wang, J.; Gao, X.; Yao, X.; Ju, J. Bioinspired Cone Structures with Helical Micro-Grooves for Fast Liquid Transport and Efficient Fog Collection. *J. Mater. Chem. A* **2023**, *11* (23), 12080–12088. https://doi.org/10.1039/D3TA01839C.
(41) Aliabadi, M.; Zarkesh, A.; Siampour, H.; Abbasian, S.; Mahdavinejad, M.; Moshaii, A. Bioinspired Azimuthally Varying Nanoscale Cu Columns on Acupuncture Needles for Fog Collection. *ACS Appl. Nano Mater.* **2021**, *4* (9), 8733.
(42) Shome, A.; Das, A.; Borbora, A.; Dhar, M.; Manna, U. Role of Chemistry in Bio-Inspired Liquid Wettability. *Chem. Soc. Rev.* **2022**, *51* (13), 5452–5497. https://doi.org/10.1039/D2CS00255H.
(43) Li, C.; Kim, B.; Yoon, J.; Sett, S.; Oh, J. Advances in Directional Wetting Surfaces for Enhanced Fluid Control: A Comprehensive Review. *Adv. Funct. Mater.* **2024**, *34* (9), 2308265. https://doi.org/10.1002/adfm.202308265.
(44) Li, K.; Ju, J.; Xue, Z.; Ma, J.; Feng, L.; Gao, S.; Jiang, L. Structured Cone Arrays for Continuous and Effective Collection of Micron-Sized Oil Droplets from Water. *Nat. Commun.* **2013**, *4* (1), 2276. https://doi.org/10.1038/ncomms3276.
(45) Chen, C.; Chen, S.; Chen, L.; Yu, Y.; Weng, D.; Mahmood, A.; Wang, J.; Parkin, I. P.; Carmalt, C. J. Underoil Superhydrophilic Metal Felt Fabricated by Modifying Ultrathin Fumed Silica Coatings for the Separation of Water-in-Oil Emulsions. *ACS Appl. Mater. Interfaces* **2020**, *12* (24), 27663–27671. https://doi.org/10.1021/acsami.0c03801.
(46) Tang, X.; Liu, H.; Xiao, L.; Zhou, M.; Bai, H.; Fang, J.; Cui, Z.; Cheng, H.; Li, G.; Zhang, Y.; Cao, M. A Hierarchical Origami Moisture Collector with Laser-Textured Microchannel Array for a Plug-and-Play Irrigation System. *J. Mater. Chem. A* **2021**, *9* (9), 5630–5638. https://doi.org/10.1039/D0TA11975J.
(47) Ma, H.; Cao, M.; Zhang, C.; Bei, Z.; Li, K.; Yu, C.; Jiang, L. Directional and Continuous Transport of Gas Bubbles on Superaerophilic Geometry-Gradient Surfaces in Aqueous Environments. *Adv. Funct. Mater.* **2018**, *28* (7), 1705091. https://doi.org/10.1002/adfm.201705091.
(48) Hirai, Y.; Mayama, H.; Matsuo, Y.; Shimomura, M. Uphill Water Transport on a Wettability-Patterned Surface: Experimental and Theoretical Results. *ACS Appl. Mater. Interfaces* **2017**, *9* (18), 15814–15821. https://doi.org/10.1021/acsami.7b00806.
(49) Feng, S.; Wang, S.; Gao, L.; Li, G.; Hou, Y.; Zheng, Y. Controlled Directional Water-Droplet Spreading on a High-Adhesion Surface. *Angew. Chem. Int. Ed.* **2014**, *53* (24), 6163–6167. https://doi.org/10.1002/anie.201403246.

View Article Online
DOI: 10.1039/D5NR02015H

Data Availability Statement

The data supporting this article have been included as part of the ESI.

Electronic supplementary information (ESI) available. See DOI: XXXX